

Di-Higgs signatures from R-parity violating supersymmetry as the origin of neutrino mass

Sanjoy Biswas¹, Eung Jin Chun¹ and Pankaj Sharma²

¹ *Korea Institute for Advanced Study, Seoul 130-722, Korea*

² *Center of Excellence in Particle Physics (CoEPP),
The University of Adelaide, Adelaide, Australia*

Abstract

Motivated by the naturalness and neutrino mass generation, we study a bilinear R-parity violating supersymmetric scenario with a light Higgsino-like lightest supersymmetric particle (LSP). We observe that the LSP dominantly decays to νh in a large part of the parameter space, and thus study the pair production of electroweakinos followed by the decays $\tilde{\chi}_1^\pm \rightarrow \tilde{\chi}_1^0 W^{\pm*}$ and $\tilde{\chi}_1^0 \rightarrow \nu h$. This leads to an interesting signature of Higgs boson pair production associated with significantly large missing transverse energy which is grossly distinct from the di-Higgs production in the Standard Model. We investigate the perspective of probing such signatures by performing a realistic detector level simulation of both the signal and corresponding backgrounds for the high-luminosity high energy phase of the Large Hadron Collider (LHC). We also advocate some observables based on kinematical features to provide an excellent handle to suppress the backgrounds.

1 Introduction

Supersymmetry (SUSY) has been considered as the best framework to protect the electroweak scale from the quadratic divergence caused by a certain ultra-violet (UV) physics. As a bonus, supersymmetry provides a good candidate of dark matter of the Universe: the lightest supersymmetric particle (LSP) which is neutral and stabilized by assuming R-parity conservation. On the other hand, R-parity violation (RpV) brings another interesting possibility of generating tiny neutrino masses [1, 2] in the context of the Minimal Supersymmetric Standard Model (MSSM). The observed neutrino masses and mixings determine the lepton flavor structure of R-parity violating couplings which typically leads to clean signature of same-sign dileptons and predicts specific leptonic branching ratios of the LSP decay $\tilde{\chi}_1^0 \rightarrow l^\pm W^\mp$ [3, 4, 5, 6].

As no hint for supersymmetry appeared yet at the Large Hadron Collider (LHC), the naturalness argument for the TeV scale SUSY is in question due to a severe fine-tuning which turns out to be much more than expected. The electroweak symmetry breaking in SUSY requires a potential minimization condition:

$$\frac{m_Z^2}{2} = \frac{m_{H_d}^2 - m_{H_u}^2 \tan^2 \beta}{\tan^2 \beta - 1} - \mu^2 \quad (1)$$

where $m_{H_{u,d}}$ are the soft masses of the two Higgs doublets, $\tan \beta \equiv v_u/v_d$ is the ratio of their vacuum expectation values, and μ is the Higgs bilinear parameter in the superpotential. As the LHC pushes up the soft mass scale above TeV range, the condition (1) requires a fine cancellation among different terms. Barring too huge cancellation, one may arrange $m_{H_{u,d}}$ and μ not too larger than m_Z [7], which still remains a viable option for SUSY. It is a challenge for the LHC and future colliders to probe such a degenerate electroweakino [8].

In this paper, we investigate the LHC signatures of the light Higgsino in association with bilinear R-parity violation (BRpV) as the origin of the observed neutrino masses and mixings. Contrary to the conventional studies on BRpV predicting a peculiar signature of same-sign dileptons from $pp \rightarrow \tilde{\chi}_1^0 \tilde{\chi}_1^0 \rightarrow l^\pm l^\pm W^\mp W^\mp$, we will focus on the unusual case of the Higgsino LSP decay dominated by the Higgs channel $\tilde{\chi}_1^0 \rightarrow \nu h$ which will be shown to occur in a large region parameter space of the scenario under consideration. As a consequence, it leads to an interesting LHC signature of di-Higgs bosons with missing transverse energy. Measurement of Higgs-pair production cross-section will be one of the main focuses of the high energy and high luminosity LHC run. It is also an important step towards our understanding of the electroweak symmetry breaking mechanism. At LHC energies, Higgs boson pair production occurs dominantly through the gluon fusion in the SM [9]. Other processes, such as weak boson fusion $qq^{(\prime)} \rightarrow qq^{(\prime)} hh$, associated

productions $q\bar{q}^{(\prime)} \rightarrow Whh$, Zhh or associated production with top quarks, $gg, q\bar{q} \rightarrow t\bar{t}hh$ also occur albeit with cross sections which are 10-30 times smaller than the gluon fusion [10, 19]. Di-Higgs production at the LHC has been studied in the context of trilinear Higgs self coupling measurements by various authors [11] and references there in. While the SM cross sections are too small to allow observation at the LHC, it also plays a crucial role in the context of new physics searches at the LHC since physics beyond the SM can lead to an enhancement of the observable cross sections and/or different event kinematics. We demonstrate that di-Higgs in association with a large \cancel{E}_T can be very useful to probe the BRpV SUSY where conventional channels fail to be sensitive. Assuming only the electroweak production of the electroweakino pairs, we analyze the di-Higgs signal in the channel of $\gamma\gamma b\bar{b}\cancel{E}_T$ at the LHC14 with the integrated luminosity ranging from 1-3 ab^{-1} . Search for Higgs-pair production as a window to probe new physics is one of the major activities in the context of LHC and future collider, *e.g.*, resonant Higgs-pair production in the context of singlet and doublet extension of the SM [12, 13], double Higgs production via gluon fusion in the effective field theory framework [14], Higgs pair production in the context of SUSY extension of the SM [15, 16, 17] and various other extensions of it [18].

This paper is organized as follows: In Section 2 summarizing the results of Refs. [4, 6], we provide a brief review on the bilinear RpV couplings constrained by the resulting tree-level neutrino mass matrix. In Section 3, the Higgsino-like LSP decay modes are analyzed for the cases of $\mu < M_1 \leq M_2$ where $M_{1,2}$ are the masses of the bino and wino components, respectively. In Section 4, we compute the Higgsino pair production cross-section for some benchmark points and perform a realistic detector-level simulation for signals and backgrounds in the di-Higgs decay channel of $hh \rightarrow \gamma\gamma b\bar{b}$ and obtain the LHC14 perspective to probe our scenario. Finally, we summarize our results and conclude in Section 5. In Appendix A, we collect the effective R-parity violating couplings relevant for the Higgsino decays and Appendix B shows the decay widths of the neutralinos induced by the BRpV couplings.

2 Bilinear RpV and neutrino mass matrix

Allowing lepton number violation in the supersymmetric standard model, the superpotential is composed of the R-parity conserving W_0 and violating W_1 part;

$$\begin{aligned}
W_0 &= \mu H_1 H_2 + h_{ij}^e L_i H_2 E_j^c + h_{ij}^d Q_i H_2 D_j^c + h_{ij}^u Q_i H_1 U_j^c \\
W_1 &= \epsilon_i \mu L_i H_1 + \frac{1}{2} \lambda_{ijk} L_i L_j E_k^c + \lambda'_{ijk} L_i Q_j D_k^c.
\end{aligned} \tag{2}$$

Among soft supersymmetry breaking terms, let us write R-parity violating bilinear terms;

$$V_{soft} = B\mu H_1 H_2 + B_i \epsilon_i \mu L_i H_1 + m_{L_i H_2}^2 L_i H_2^\dagger + h.c. . \quad (3)$$

It is clear that the electroweak symmetry breaking gives rise to nonzero vacuum expectation values of sneutrino fields, $\tilde{\nu}_i$, as follows:

$$a_i \equiv \frac{\langle \tilde{\nu}_i \rangle}{\langle H_2 \rangle} = -\frac{\bar{m}_{L_i H_2}^2 + B_i \epsilon_i \mu t_\beta}{m_{\tilde{\nu}_i}^2} \quad (4)$$

where $\bar{m}_{L_i H_2}^2 = m_{L_i H_2}^2 + \epsilon_i \mu^2$, $t_\beta = \tan \beta = \langle H_1 \rangle / \langle H_2 \rangle$ and $m_{\tilde{\nu}_i}^2 = m_{L_i}^2 + M_Z^2 c_{2\beta} / 2$.

Given the BRpV couplings ϵ_i and a_i , the neutrino-neutralino sector form a 7×7 mass matrix whose 3×4 (Dirac) neutrino-neutralino mass matrix takes the form of

$$\mathcal{M}_{ij}^D = (-a_i c_\beta M_Z s_W, a_i c_\beta M_Z c_W, 0, \epsilon_i \mu) \quad (5)$$

where $s_W \equiv \sin \theta_W$ is the weak mixing angle, and the index i runs for three neutrino flavors (ν_e, ν_μ, ν_τ), and j runs for the neutralino states ($\tilde{B}, \tilde{W}_3, \tilde{H}_1^0, \tilde{H}_2^0$) which has the usual 4×4 mass matrix \mathcal{M}^N containing the bino, wino and Higgsino masses denoted by M_1, M_2 and μ , respectively.

As is well-known, a seesaw diagonalization rotating away \mathcal{M}^D [see Appendix A for details] generates the ‘‘tree-level’’ neutrino mass matrix $\mathcal{M}^\nu = -\mathcal{M}^D \mathcal{M}^{N-1} \mathcal{M}^{D^T}$ whose components are given by

$$\mathcal{M}_{ij}^\nu = -\frac{M_Z^2}{F_N} \xi_i \xi_j c_\beta^2, \quad (6)$$

where $\xi_i \equiv a_i - \epsilon_i$ and $F_N = M_1 M_2 / (c_W^2 M_1 + s_W^2 M_2) + M_Z^2 s_{2\beta} / \mu$. This makes massive only one neutrino, ν_3 , in the direction of $\vec{\xi}$. The other two get masses from finite one-loop corrections and thus ν_3 is usually the heaviest component. We fix the value of m_{ν_3} from the atmospheric neutrino data and thus the overall size of $\xi \equiv |\vec{\xi}|$ is determined to be

$$\xi c_\beta = 0.74 \times 10^{-6} \left(\frac{F_N}{M_Z} \right)^{1/2} \left(\frac{m_{\nu_3}}{0.05 \text{ eV}} \right)^{1/2}. \quad (7)$$

Furthermore, among three neutrino mixing angles defined by the mixing matrix

$$U = \begin{pmatrix} 1 & 0 & 0 \\ 0 & c_{23} & s_{23} \\ 0 & -s_{23} & c_{23} \end{pmatrix} \begin{pmatrix} c_{13} & 0 & s_{13} \\ 0 & 1 & 0 \\ -s_{13} & 0 & c_{13} \end{pmatrix} \begin{pmatrix} c_{12} & s_{12} & 0 \\ -s_{12} & c_{12} & 0 \\ 0 & 0 & 1 \end{pmatrix} \quad (8)$$

with $c_{ij} = \cos \theta_{ij}$ and $s_{ij} = \sin \theta_{ij}$, etc., two angles are determined by the tree-level mass matrix (6) as follows:

$$\begin{aligned} \sin^2 2\theta_{23} &\approx 4 \frac{\xi_2^2 \xi_3^2}{\xi^2 \xi^2} \\ \sin^2 2\theta_{13} &\approx 4 \frac{\xi_1^2}{\xi^2} \left(1 - \frac{\xi_1^2}{\xi^2} \right). \end{aligned} \quad (9)$$

These two angles define the atmospheric and reactor neutrino oscillation angles, respectively, and thus one has $\sin^2 2\theta_{23} \approx 1$ and $\sin^2 2\theta_{13} \approx 0.09$ [20]. This implies that the sizes of ξ_i should follow the relation:

$$|\xi_1| : |\xi_2| : |\xi_3| \approx 0.1 : 1 : 1. \quad (10)$$

The other angle θ_{12} can be determined only after including one-loop corrections which are assumed to be smaller than the tree-level contribution (6) and thus irrelevant for our discussion.

The BRpV terms induce mixing between neutrinos (charged leptons) and neutralino (charginos) as well as their scalar partners. Rotating them away, one gets the effective RpV vertices of neutralinos and charginos which are summarized in Appendix A.

3 Light Higgsino Decays

A distinct feature of the RpV SUSY models is that the LSP, $\tilde{\chi}_1^0$, is not stable. In our analysis, neutralino decays via sfermions are highly suppressed in the limit of heavy sfermion masses and small trilinear RpV couplings responsible for one-loop neutrino mass generation. Therefore, we discuss the branching ratios (BR) of the LSP for the following decay processes:

$$\tilde{\chi}_1^0 \rightarrow Z\nu_\ell, \quad \tilde{\chi}_1^0 \rightarrow \ell W, \quad \tilde{\chi}_1^0 \rightarrow h\nu_\ell \quad (11)$$

where ℓ is any of the three charged-leptons.

To explore the phenomenological features, we consider a specific scenario in this work where $\mu < M_1, M_2$ leading to a situation of the Higgsino LSP, with the lightest states $\tilde{\chi}_{1,2}^0$ and $\tilde{\chi}_1^\pm$ being Higgsino-like. If $M_1 < M_2$, $\tilde{\chi}_3^0$ is bino-like while $\tilde{\chi}_2^\pm$ and $\tilde{\chi}_4^0$ are wino-like; and for $M_2 < M_1$, $\tilde{\chi}_4^0$ is bino-like while $\tilde{\chi}_2^\pm$ and $\tilde{\chi}_3^0$ are wino-like.

In the following, we fix $M_1 = 1.0$ TeV and vary both μ and M_2 . Given M_1 and M_2 , the masses of electroweakinos are determined by the value of μ . We also vary $\tan\beta$ to see the variation of branching ratios with respect to μ , M_2 and $\tan\beta$ (Fig. 1). Fig. 1 shows that the branching ratio for the ℓW or νh decay mode is quite sensitive to the values of μ , M_2 and $\tan\beta$.

All of the RpV vertices which we have obtained in Eqs. 18-23 of Appendix A depend only on one type of BRpV variables ξ_i which have taken to satisfy $\xi_1 : \xi_2 : \xi_3 = 0.1 : 1 : 1$ (Eq. 10). Thus, $\text{BR}(\tilde{\chi}_1^0 \rightarrow eW)$ is quite suppressed and major contribution to ℓW mode comes from μW and τW channels. An important point to note is that the decay rate ($\tilde{\chi}_1^0 \rightarrow \ell W$) also depends on charged-lepton masses through c_2^R (Eq. 26). Although this mass dependence is suppressed by m^ℓ/F_C , its contribution can be substantial for τ -lepton

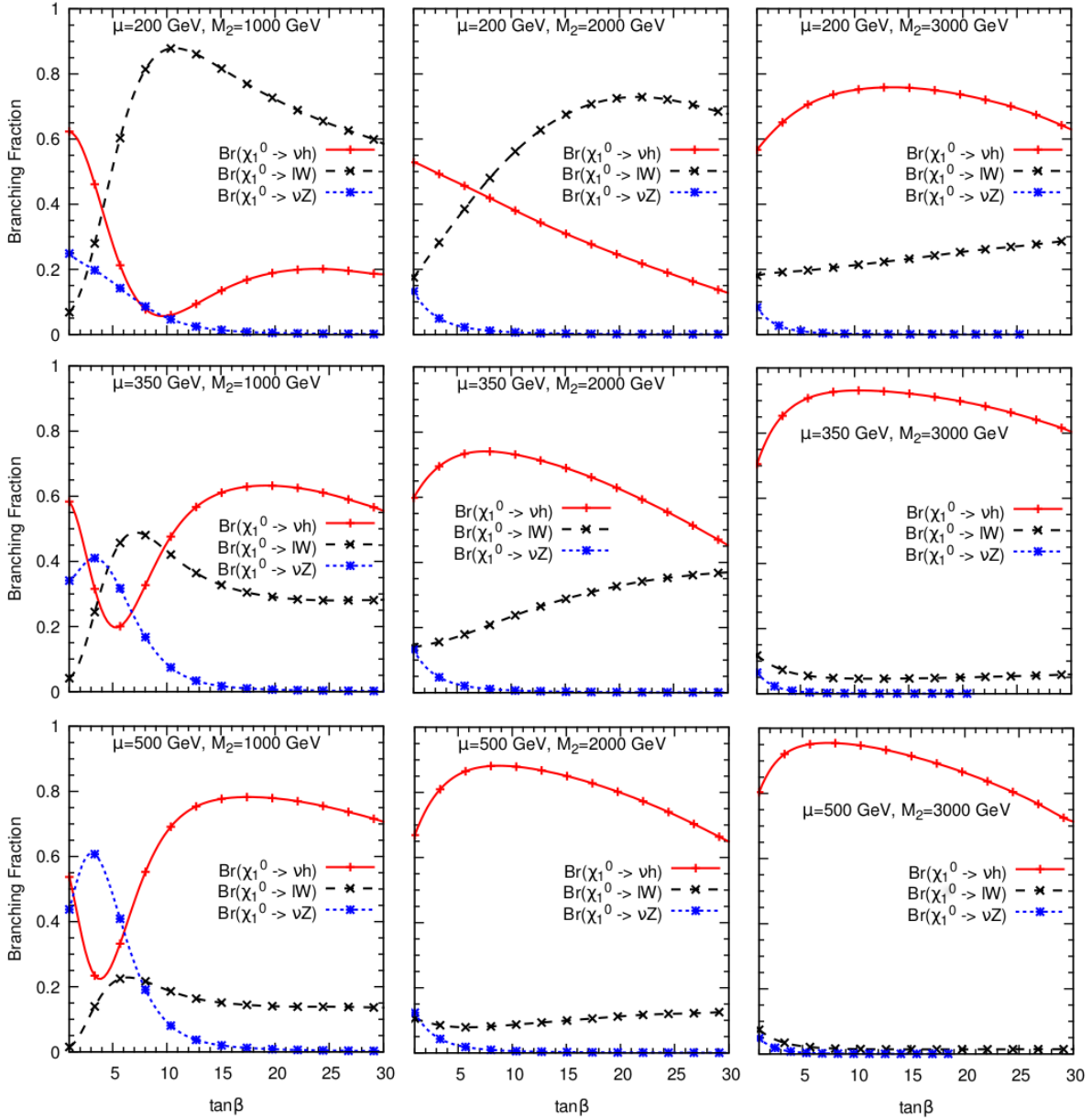


Figure 1: Branching fractions for the decays $\tilde{\chi}_1^0 \rightarrow \nu h$, $\tilde{\chi}_1^0 \rightarrow \ell W$ and $\tilde{\chi}_1^0 \rightarrow \nu Z$ in terms of $\tan\beta$ for different values of μ and M_2 .

at large $\tan\beta$ as c_2^R is proportional to $\tan\beta$ (Eq. 16). Thus, $\text{BR}(\tilde{\chi}_1^0 \rightarrow \ell W)$ grows at large $\tan\beta$ through the enhancement of τW decay width.

Another important aspect to note from Eq. 16 is that both c_i^L and c_i^R are inversely proportional to μ . Thus for small values of μ , the decay rate $\Gamma(\tilde{\chi}_1^0 \rightarrow \ell W)$ is much larger than νZ and νh decay modes. This feature can be seen from the top row of Fig. 1 where we have displayed the BRs of ℓW , νh and νZ decay modes for $\mu = 200$ GeV. In these

figures, it can be seen that $\text{BR}(\ell W)$ dominates at large $\tan\beta$. Decay mode νh is only significant at low $\tan\beta$. For larger value of $\mu = 500$ GeV (see bottom panel of Fig. 1), $\text{BR}(\ell W)$ becomes subdominant as expected. Thus, the dominant decay channel with the branching ratio varying between (0.6-0.9) is the νh mode for all values of $\tan\beta$. $\text{BR}(\nu h)$ decreases by about 20% because of the increase in the decay rate of $\tilde{\chi}_1^0 \rightarrow \ell W$ at large $\tan\beta$.

From the Fig. 1, we conclude that for large $M_2 = 3$ TeV, the $\text{BR}(\tilde{\chi}_1^0 \rightarrow \nu h)$ always dominates over all other $\tilde{\chi}_1^0$ decays. For moderate $M_2 = 2$ TeV, the $\text{BR}(\tilde{\chi}_1^0 \rightarrow \nu h)$ still dominates over ℓW and νZ modes but for low values of $\tan\beta$ while for small $M_2 = 1$ TeV, we find that $\text{BR}(\tilde{\chi}_1^0 \rightarrow \nu h)$ dominates but only for large value of $\tan\beta$ and for large values of μ . All these facts can easily be deduced from the effective RpV couplings which are derived in Appendix A. To have better understanding of the behavior of $\text{BR}(\tilde{\chi}_1^0 \rightarrow \nu h)$, we plot the BR in the plane of (M_2, μ) for three different values of $\tan\beta = 5$ (left), 15 (center) and 25 (right) in Fig. 2. One can see from the Fig. that the largest possible values of the $\text{BR}(\tilde{\chi}_1^0 \rightarrow \nu h)$ can be achieved when $\tan\beta$ is small and both M_2 and μ is large.

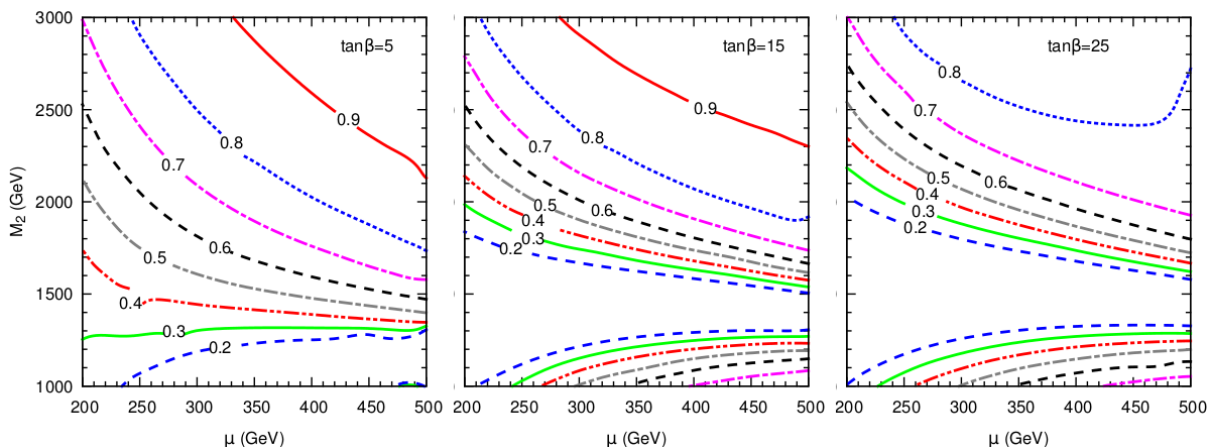


Figure 2: Branching ratio of the decay $\tilde{\chi}_1^0 \rightarrow \nu h$ in the $M_2 - \mu$ plane for three different values of $\tan\beta = 5$ (left), 15 (center) and 25 (right).

4 Light Higgsino production at the LHC

From the analysis of previous section, we conclude that the decay channel $\tilde{\chi}_1^0 \rightarrow \nu h$ is significant in large part of the parameter space and, in fact, close to $\sim 90 - 95\%$ in certain regions. Motivated by this observation, we consider a very interesting signature of Higgs

boson pair-production at the LHC in RpV SUSY. To probe this yet unexplored parameter space through di-Higgs, we consider pair production of Higgsinos at the 14 TeV LHC run:

1. Neutralino pair production: $pp \rightarrow \tilde{\chi}_1^0 \tilde{\chi}_i^0$,
2. Chargino pair production : $pp \rightarrow \tilde{\chi}_1^+ \tilde{\chi}_1^-$,
3. Associated neutralino and chargino production : $pp \rightarrow \tilde{\chi}_1^\pm \tilde{\chi}_i^0$,

where $i = 1, 2$. The main contributions to these processes come from s -channel mediation of γ , Z and W^\pm bosons (see Fig. 3). The contributions from t -channel squark mediated processes are suppressed by heavy squark masses and can be ignored. Hence, the cross sections only depend on the masses of the electroweak gauginos and their couplings with γ , Z and W^\pm bosons. We have worked with leading order (LO) cross-sections. The effects of next-to-leading order (NLO) QCD corrections can be achieved by including multiplicative K factors which can give a 10-20% enhancement. However, here we present a conservative estimate without multiplying by any K-factors. In Fig. 4, we show the cross sections for these production channels as a function of μ at 14 TeV LHC. The cross sections for the associated production are the largest followed by the chargino and neutralino pair productions.

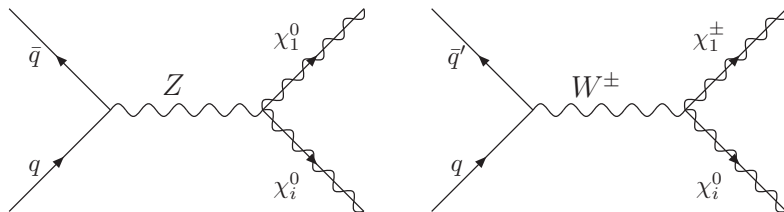


Figure 3: Feynman diagrams representing pair production of electroweakinos. Similar diagram for chargino pair production mediated via γ^* and Z boson also exist.

The chargino mainly decays via R-parity conserving coupling to $\tilde{\chi}_1^\pm \rightarrow \tilde{\chi}_1^0 W^{\pm*} \rightarrow f f' \tilde{\chi}_1^0$ almost 90% of time in all regions of the parameter space. The R-parity violating decays ($\ell h, \nu W, \ell Z$) are suppressed compared to the R-parity conserving one due to the tiny RPV couplings. Thus, in most of the events, one ends up with a pair of LSP's which subsequently decays to $\tilde{\chi}_1^0 \rightarrow \nu h$ via R-parity violating interactions. This naturally leads to pair production of Higgs and two invisible neutrinos which contribute to missing transverse energy (\cancel{E}_T). The signal we investigate at the LHC, therefore, consists of $pp \rightarrow hh + \cancel{E}_T + X$, where X stands for additional jets and/or unclustered particles but no isolated leptons.

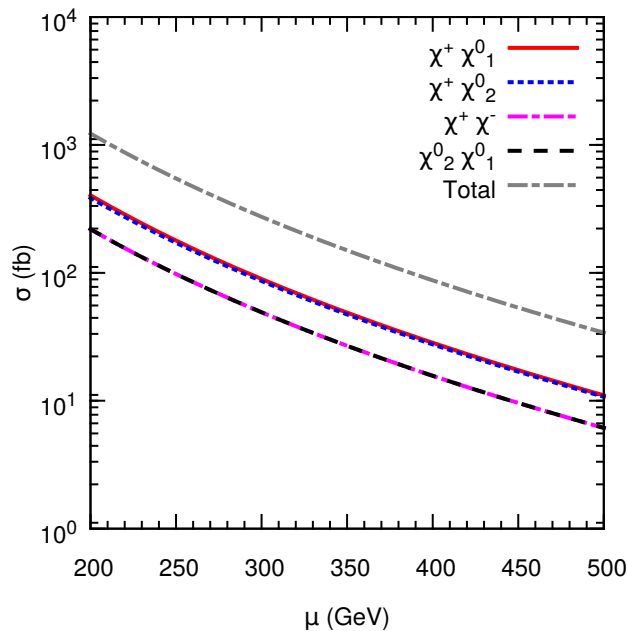


Figure 4: Production cross sections of the charged and neutral Higgsinos in terms of μ at the LHC14.

In Table 1, we show the branching ratios of di-Higgs decays in various channels. The dominant decay of the SM-like Higgs to a pair of b quarks occurs with a branching ratio of 60%. Thus, the dominant branching ratio for di-Higgs decay is to $hh \rightarrow bbbb$, which is $\sim 36\%$. But the backgrounds for $4b$ and $2b2\tau$ final states are overwhelming. While the backgrounds for 4τ decay mode are moderate, it suffers from small τ detection efficiencies. As far as decays to electroweak gauge bosons are concerned, $bbWW$ and $bbZZ$ decaying to $b\bar{b}\ell^+\ell^-\nu\bar{\nu}$ suffer from huge QCD $t\bar{t}$ pair backgrounds. The $b\bar{b}ZZ^* \rightarrow b\bar{b} + 4$ leptons and $b\bar{b}Z\gamma$ channels suffer from too small rates. So, this leaves us a very few options to choose from. Among all the di-Higgs decay channels, we focus on the possibility where one Higgs decays to a $b\bar{b}$ pair and the other to a di-photon pair. Thus the final signature for di-Higgs search of interest in this work is $\gamma\gamma b\bar{b}\cancel{E}_T + X$ at the LHC.

We generate the spectrum for the BRpV SUSY model using SARAH [21] and SPheno [22], and then, use these spectrum files in the PYTHIA [23] to generate the events. We also use PYTHIA for the parton showering and hadronisation. We have used simple cone algorithm of PYCELL inside PYTHIA to form jets out of clusters of hadrons with a cone size of $R = 0.4$. For a realistic detector simulation, we also include the appropriate Gaussian smearing of the energies of each objects (i.e., jets and photon) in an event using the

Channel	BR(%)
bbbb	36
bbWW	24.7
bb $\tau\tau$	7.3
WWWW	4.3
bb $\gamma\gamma$	0.27
bbZZ($\rightarrow e^+e^-\mu^+\mu^-$)	0.015
$\gamma\gamma\gamma\gamma$	0.00052

Table 1: Branching ratios for different di-Higgs channels.

following resolution function,

$$\frac{\Delta E}{E} = \frac{a}{E} \oplus \frac{b}{\sqrt{E}} \oplus c.$$

For jets, we take $a = 1$ GeV, $b = 0.8$ GeV^{1/2}, $c = 0.05$ while for photons the values are $a = 0.35$ GeV, $b = 0.07$ GeV^{1/2}, $c = 0.007$ [24, 25]. Here, E is in the units of GeV. The identification efficiencies for a true b -jet, photon and their respective mistagging probabilities have been given in Table 2. The tagging and mistagging efficiencies are more or less consistent with the ATLAS experiment and have been taken from [26].

In the following, we will perform a detailed collider simulation for the di-Higgs production process and the corresponding backgrounds at the 14 TeV high luminosity LHC with the luminosity of 3 ab^{-1} in the BRpV model. We will also discuss the strategy and cuts required to suppress the backgrounds and enhance the signal-to-background ratio. In our simulation, we consider different values of Higgsino masses, ranging from 200 GeV to 600 GeV, for the signal reconstruction and analysis. However for the purpose of illustration, we consider the following benchmark point for the model where $\text{BR}(\tilde{\chi}_1^0 \rightarrow \nu h)$ is maximized: $\mu = 300$ GeV, $\tan\beta = 15$, $M_2 = 3$ TeV. For this benchmark point, we have $M_{\tilde{\chi}_1^0} = 300$ GeV, $M_{\tilde{\chi}_1^\pm} = 310$ GeV, $\text{BR}(\tilde{\chi}_1^0 \rightarrow \nu h) = 0.9$, $\text{BR}(\tilde{\chi}_1^+ \rightarrow \tilde{\chi}_1^0 W^+) = 0.95$ and $\sigma(pp \rightarrow \chi\chi) = 232$ fb. We have shown all the figures for the various distribution for this benchmark point. Nevertheless we also present our analysis for various Higgsino masses in Table 3.

4.1 $\gamma\gamma b\bar{b}$ Channel

We perform the signal calculation $pp \rightarrow hh \cancel{E}_T + X \rightarrow b\bar{b}\gamma\gamma \cancel{E}_T + X$. Though the branching ratio of the $\gamma\gamma b\bar{b}$ channel is very small, it can reach the similar sensitivity of

ϵ_γ	ϵ_b	$P_{c \rightarrow b}$	$P_{\tau \rightarrow b}$	$P_{j \rightarrow b}$	$P_{j \rightarrow \gamma}$
90%	70%	1/8	1/26	1/440	1/1000

Table 2: Photon and b jet identification efficiencies and misidentification probabilities for charm quarks, τ , light jets to b jets and photons at the LHC. [26]

the $b\bar{b}WW$ channel in probing the di-Higgs signals because of the precise resolution of two photons which leads to a very prominent peak around Higgs mass in $M_{\gamma\gamma}$ distribution. The background processes for the $\gamma\gamma b\bar{b}$ channel are QCD $b\bar{b}\gamma\gamma$, $b\bar{b}h(\rightarrow \gamma\gamma)$, $\gamma\gamma h(\rightarrow b\bar{b})$ and multijet QCD backgrounds resulting from jets faking either as b -jets or photons like $jj\gamma\gamma$ with two fake b jets; $b\bar{b}j\gamma$ with j faking photon; $b\bar{b}jj$ with two fake photons; $jjj\gamma$ with two fake b jets and one fake photon; $jjjj$ with two fake b -jets and two photons; hjj with either two fake b jets or two fake photons; and $hj\gamma$ with one fake photon. While estimating and generating multijet backgrounds, we consider the misidentified charm quarks separately from the light flavour jets because of the very different mistagging factors as given in Table 2.

In the following we present our strategy to suppress the background and enhance the signal-to-background ratio. The acceptance and selection cuts applied in our analysis are as follows:

- **Identification cuts (Cut 1):**

1. Accept events with two photons, 2 b -jets and missing energy,
2. Photons must have transverse momentum $p_T^\gamma > 10$ GeV and rapidity $|\eta^\ell| < 2.5$,
3. All b -jets must have following p_T and η requirements:

$$p_T^b > 20 \text{ GeV}, |\eta^b| < 2.5$$

4. All pairs of jets, photons and photon plus jets should be well separated with each other by:

$$\Delta R_{jj,jb,bb,\gamma j,\gamma b,\gamma\gamma} \geq 0.4 \quad \text{where} \quad \Delta R = \sqrt{(\Delta\phi)^2 + (\Delta\eta)^2}$$

- **Selection requirements:** When an event satisfies above requirements, it is further processed for the signal reconstruction and background reduction as follows:

- **Cut on p_T of photons (Cut 2):** To get rid of soft photons coming from the decay of mesons or radiations, we further put the following p_T cuts on the two photons:

$$p_T^{\gamma 1} > 30\text{GeV} \quad \text{and} \quad p_T^{\gamma 2} > 20\text{GeV}.$$

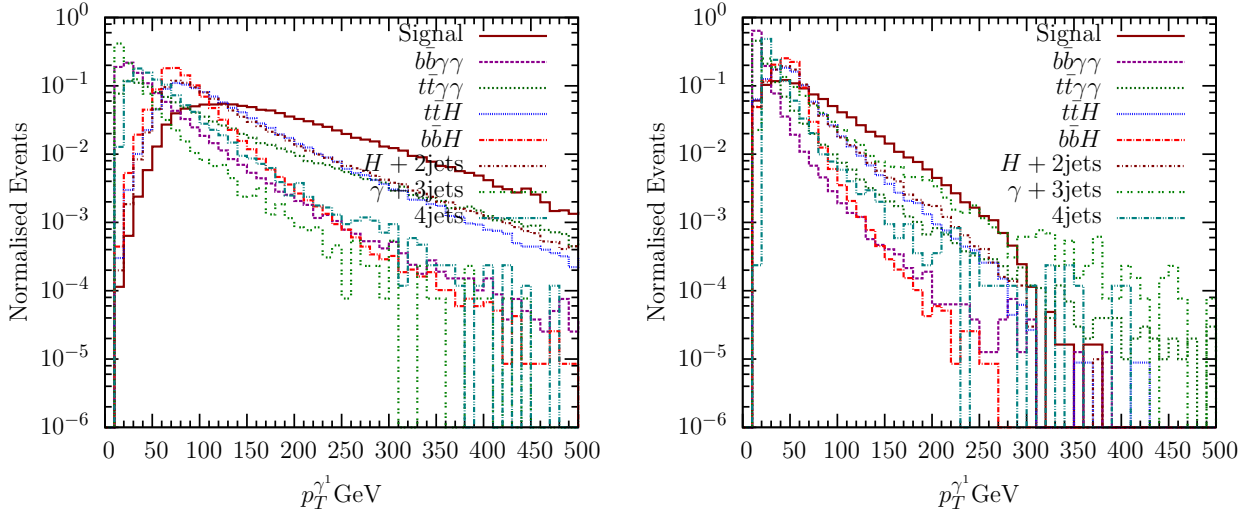


Figure 5: Transverse momentum distribution of the two photons for the signal and backgrounds.

In Fig. 5, we show the transverse momentum distribution of the two photons for the signal as well as for the backgrounds before the cuts. For the hardest photon, the distribution peaks at around 100 GeV while most backgrounds peak at low p_T .

- **Invariant mass cuts (Cut 3):** In Fig. 6, we show the invariant mass distribution of two photons, $M_{\gamma\gamma}$ and two b jets, $M_{b\bar{b}}$ for both the signal and backgrounds. In the case of the signal and some of the backgrounds, the two photons come from a resonant Higgs. Thus, the diphoton invariant mass distributions for the resonant Higgs have a very narrow peak around $M_h = 125$ GeV. On the other hand, for other backgrounds, the distribution is continuum with no localised events around M_h . Also, the fact that the photons are measured at a very high degree of precision at the LHC, allows a very sharp distribution even at the detector level. On the other hand, due to the large jet energy uncertainties and energy resolution of the jets, the invariant mass distributions of the resonant Higgs decaying to two b -jets show a relatively-wider peak. The peak is also shifted towards lower value (around 112.5 GeV) than the actual Higgs mass due to invisible neutrinos coming from b -decays and missing particles outside the jet cone. Both the diphoton and di- b -jet invariant mass distributions are quite distinct from the background and have prominent peaks. We utilize this to suppress the backgrounds and further cuts

on invariant masses are imposed:

$$|M_{\gamma\gamma} - M_h| < 2.5 \text{ GeV}, \quad |M_{b\bar{b}} - 112.5| < 15 \text{ GeV},$$

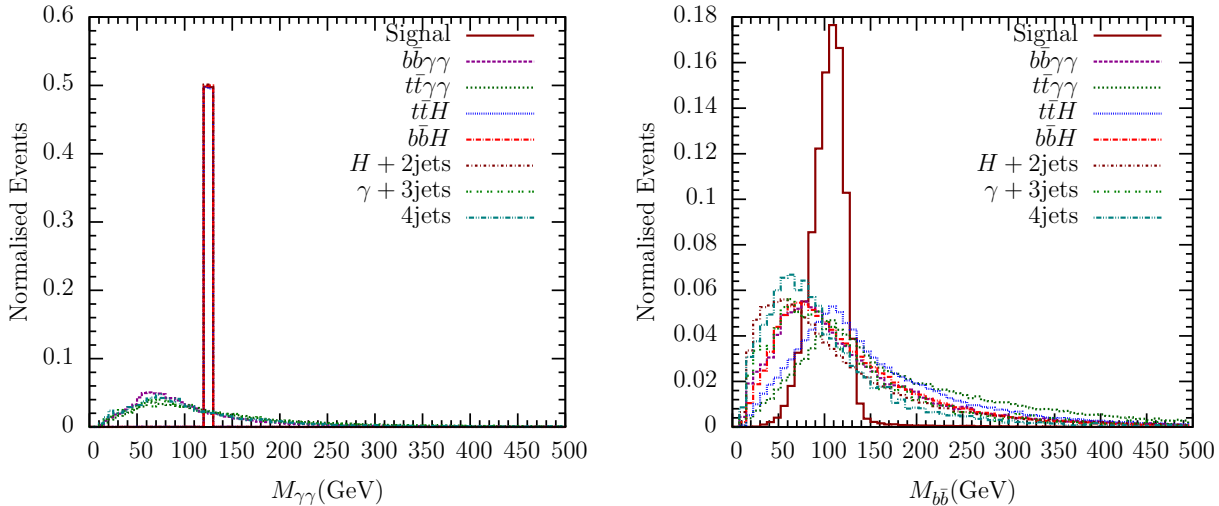


Figure 6: Invariant mass distribution for $\gamma\gamma$ and $b\bar{b}$ pairs in $b\bar{b}\gamma\gamma\cancel{E}_T$ signal for di-Higgs production process at the 14 TeV LHC.

- **Missing transverse Energy, \cancel{E}_T distribution (Cut 4):** In this analysis, the di-Higgs signal arise from the decays of two lightest neutralinos to Higgs and neutrino. The neutrinos coming from heavy particles are expected to have a large transverse momentum contributing to \cancel{E}_T . In Fig. 7, we show the \cancel{E}_T distribution for the signal as well as backgrounds. For the $M_{\chi_1^0} = 300$ GeV, the \cancel{E}_T distribution is expected to peak at around 200 GeV. For the non-top backgrounds, the only source of \cancel{E}_T comes from uncertainties in the measurements of p_T of the various objects at the detector, dominant being jets. Thus, the peaks in \cancel{E}_T distributions for such backgrounds are at very low \cancel{E}_T . On the other hand, the backgrounds, which contain top-pairs, produce neutrinos when they decay semi-leptonically and thus may have large \cancel{E}_T . From Fig. 7 we see that the \cancel{E}_T distribution for a non-top background almost vanish at (≤ 80 GeV) while the backgrounds containing a top-pair have significant \cancel{E}_T until $\cancel{E}_T < 200$ GeV. For the signal, the peak is at 200 GeV and the distribution remains significant until a very large value of $\cancel{E}_T \sim 800$ GeV. Thus, we further put a cut of

$$\cancel{E}_T > 100\text{GeV}$$

to further suppress the backgrounds. With this cut, the $b\bar{b}\gamma\gamma$ background is

completely eliminated and the total background is suppressed by a factor of 30 while the signal events are affected only by 20%.

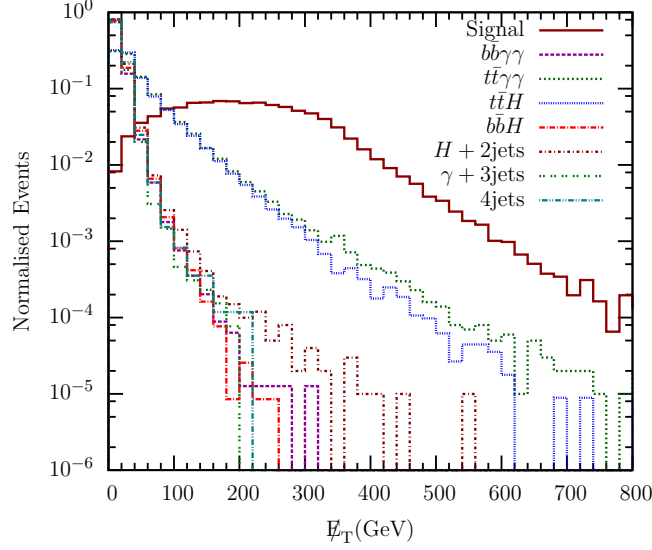


Figure 7: Missing transverse energy, \cancel{E}_T , distribution for $b\bar{b}\gamma\gamma\cancel{E}_T$ signal for the di-Higgs process and various backgrounds at the 14 TeV LHC.

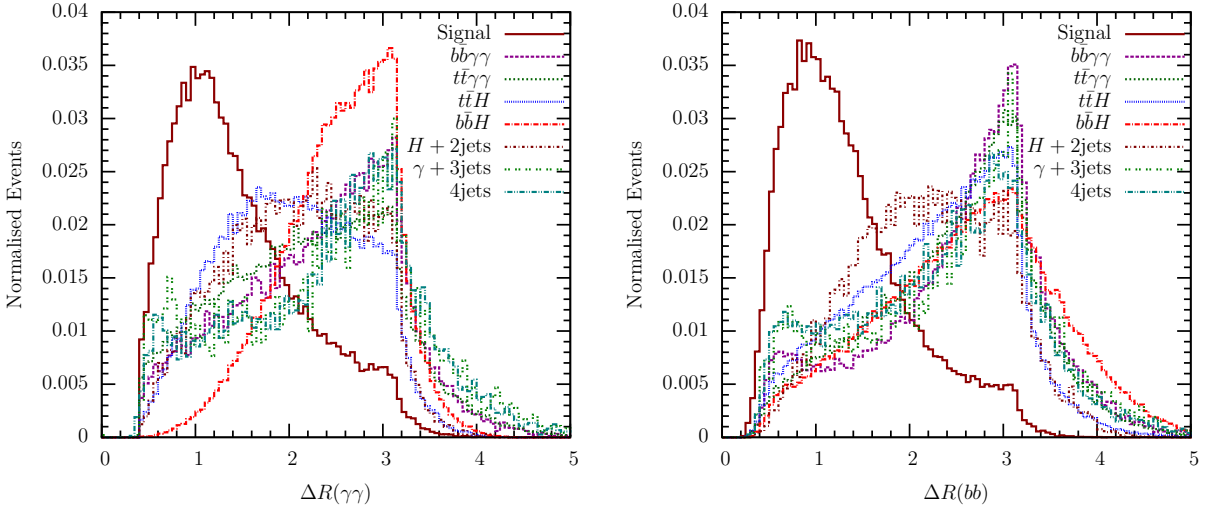


Figure 8: ΔR distribution for $\gamma\gamma$ (left) and $b\bar{b}$ pairs (right) in $b\bar{b}\gamma\gamma\cancel{E}_T$ signal for the di-Higgs process and various backgrounds at the 14 TeV LHC.

- **ΔR separation (Cut 5)**: We find two interesting angular correlations which are significantly different between signal and backgrounds. The ΔR separation of the photon-photon and $b\bar{b}$ pairs are small for the signals and larger for the backgrounds. The shape of the signal distribution stems from the fact that the

photon pair and b pair arise from the highly boosted resonant Higgs bosons. These Higgs bosons are boosted as they are produced from the decays of heavy neutralinos/charginos. On the other hand, diphotons and di- b jets for the backgrounds do not come from any heavy resonance and thus are expected to be farther spaced. This fact can be seen from Fig. 8 where we show the ΔR distribution for $\gamma\gamma$ and $b\bar{b}$ pairs. A cut on ΔR can effectively suppress the background relative to the signal. Based on these observations, we put following additional cuts:

$$\Delta R_{b\bar{b}} < 2.0, \quad \Delta R_{\gamma\gamma} < 2.0.$$

These cuts reduce the background by an order of magnitude while the signal events are reduced by only 20%.

μ (GeV)	Cut 1 (fb)	Cut 2 (fb)	Cut 3 (fb)	Cut 4 (fb)	Cut 5 (fb)
300	9.6×10^{-2}	9.0×10^{-2}	5.3×10^{-2}	3.8×10^{-2}	1.9×10^{-2}
400	3.5×10^{-2}	3.3×10^{-2}	2.0×10^{-2}	1.6×10^{-2}	1.1×10^{-2}
500	1.5×10^{-2}	1.4×10^{-2}	8.5×10^{-3}	7.6×10^{-3}	5.9×10^{-3}
600	7.1×10^{-3}	6.6×10^{-3}	4.0×10^{-3}	3.7×10^{-3}	3.2×10^{-3}

Table 3: Effects of the cut flow (discussed in Section 4.1) on the signal events. The $BR(\chi_1^0 \rightarrow \nu h)$ is assumed to be 100% for all benchmark points.

In Table 3, we show the cut flow of the cross sections for the signal for different values of the Higgsino masses. One can observe that the cross section rapidly decreases with the increase in masses but the efficiency of the cuts is better for the heavier Higgsinos. In Table 4, we show the cut flow of the cross sections for the various background processes considered in the analysis. One can see from Table 4, the dominant contributions to the background come from the $b\bar{b}\gamma\gamma$ continuum, $t\bar{t}\gamma\gamma$ and $t\bar{t}h$ processes, each having cross sections of 44 fb, 1.2 fb and 0.11 fb respectively after cut 1. On the other hand, the signal cross section after cut 1 is 0.096 fb for $M_{\tilde{\chi}^0} = 300$ GeV. Thus the signal-to-background ratio at this stage of cut flow is only 5×10^{-4} . The cut on missing transverse energy $\cancel{E}_T > 100$ GeV (cut 4) almost eliminates the $b\bar{b}\gamma\gamma$ background while the contributions of $t\bar{t}\gamma\gamma$ and $t\bar{t}h$ are reduced to 10^{-4} and 10^{-3} respectively. After the cut 4, the S/B ratio is 6 which is a tremendous improvement over previous value after cut 1. The cut 5 (on ΔR) further suppresses the background contribution and thus enhancing the S/B ratio. We estimate the statistical significance of the signal using following formula [27]

	Cut 1 (fb)	Cut 2 (fb)	Cut 3 (fb)	Cut 4 (fb)	Cut 5 (fb)
$b\bar{b}\gamma\gamma$	4.3×10^1	1.3×10^1	4.5×10^{-2}	2.1×10^{-4}	1.0×10^{-4}
$Hb\bar{b}$	9.5×10^{-3}	9.0×10^{-3}	1.5×10^{-3}	1.0×10^{-6}	4.8×10^{-7}
Hjj	2.9×10^{-5}	2.8×10^{-5}	5.5×10^{-6}	1.1×10^{-8}	1.0×10^{-8}
$t\bar{t}\gamma\gamma$	1.2×10^0	6.1×10^{-1}	2.2×10^{-3}	2.5×10^{-4}	4.7×10^{-5}
$t\bar{t}H$	1.1×10^{-1}	1.0×10^{-1}	2.0×10^{-2}	1.9×10^{-3}	5.0×10^{-4}
$b\bar{b}jj$	4.2×10^1	3.5×10^1	1.5×10^{-1}	1.6×10^{-3}	4.0×10^{-4}
$jj\gamma\gamma$	9.3×10^{-2}	2.6×10^{-2}	8.9×10^{-5}	—	—
$jjjj$	1.8×10^{-2}	1.5×10^{-2}	5.6×10^{-5}	—	—
Σ (bckg.)					1.1×10^{-3}

Table 4: Effects of the cut flow on the background events.

$$Sig = \sqrt{2((S + B)\ln(1 + \frac{S}{B}) - S)} \quad (12)$$

where S and B are the number of signal and background events, respectively.

We will now comment on the possibility of detecting the di-Higgs signal for different masses of the Higgsinos. In Table 5, we show the cut efficiency of the signal for different masses of Higgsinos. As the masses increase, the total production cross section goes down rapidly, but the handle over the background improves significantly. Thus, even though the cross section for the signal is decreased with the mass, the efficiency for the detection of the signal is increased.

μ (GeV)	Cut efficiency (%)
200	1.32
300	4.48
400	6.76
500	8.50
600	9.62

Table 5: The cut efficiencies for the signal for different Higgsino masses at the 14 TeV LHC.

Let us now look at the various distributions discussed earlier, for the different values of Higgsino masses. In Fig. 9, we show the missing transverse energy (\cancel{E}_T) distribution for the di-Higgs signal for different values of the Higgsino masses ranging from 200 GeV to 600 GeV. We notice that the \cancel{E}_T distribution peaks at 60 GeV, 100 GeV, 150 GeV, 200 GeV and 250 GeV for $M_{\chi^\pm} = 200$ GeV, 300 GeV, 400 GeV, 500 GeV and 600 GeV, respectively. Thus, in order to further improve the cut efficiency, optimizing of the cuts on \cancel{E}_T should be performed for different Higgsino masses. However, one should keep in mind that as the backgrounds are already low, any further stringent cuts would also result in reducing the signal events.

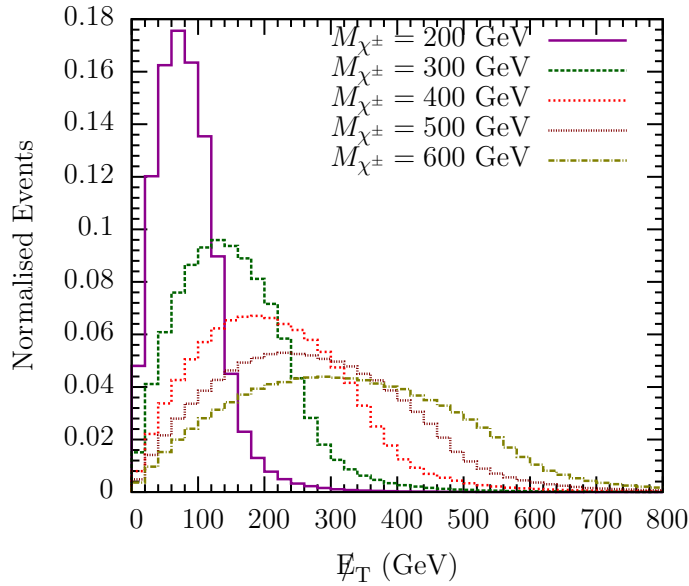


Figure 9: The \cancel{E}_T distribution for the di-Higgs process for different values of chargino masses at the 14 TeV LHC.

In Fig. 10, the ΔR separation between the photon-photon (left) and $b\bar{b}$ pairs (right) for the di-Higgs+ \cancel{E}_T signal at the 14 TeV LHC have been shown. For very heavy Higgsinos, the Higgs coming from the decay will be highly boosted. Thus the ΔR separation between $b\bar{b}/\gamma\gamma$ becomes very small. This fact determines the shape of the ΔR distributions for different chargino masses. For the mass of 600 GeV, the distribution is peaked at a very low value of ΔR while for a light chargino of 200 GeV, the diphotons and di- b jets are much farther spaced. Based on these findings, the cuts on ΔR need to be judiciously chosen so as to enhance the signal-to-background ratio for the different values of Higgsino masses.

We now discuss the exclusion/discovery limits for the Higgsino LSP in di-Higgs production at the LHC14 for the different values of integrated luminosities. Based on the

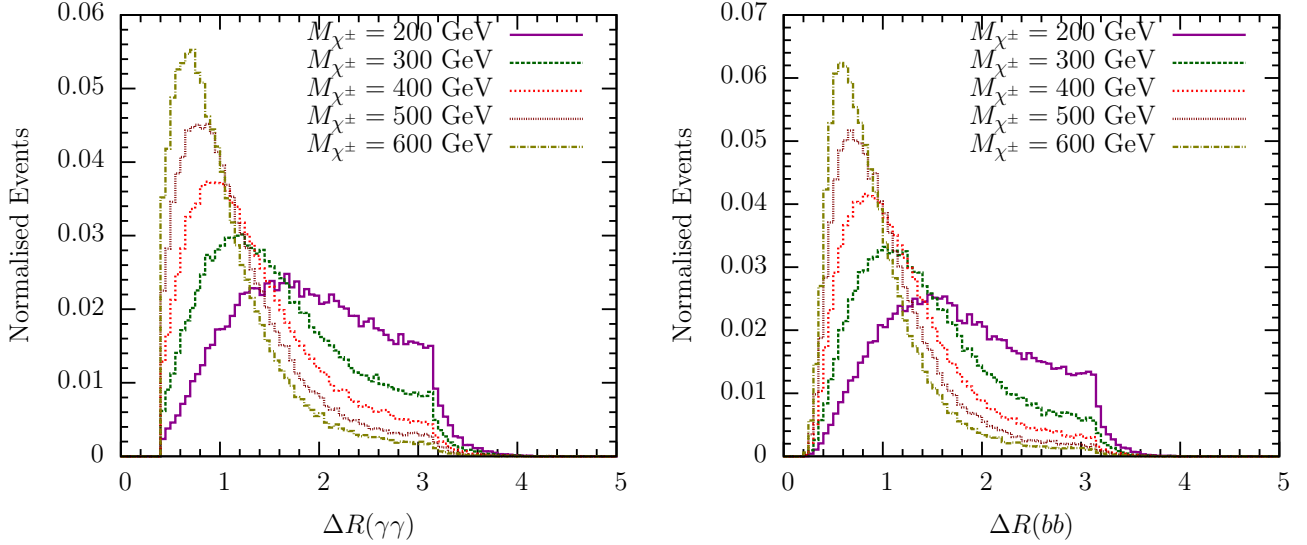


Figure 10: The ΔR distribution for $\gamma\gamma$ (left) and $b\bar{b}$ pairs (right) for the di-Higgs process for different values of chargino masses at the 14 TeV LHC.

μ (GeV)	Sig. (1 ab^{-1})	Sig. (2 ab^{-1})	Sig. (3 ab^{-1})
300	10.3	14.6	17.2
400	6.6	9.3	11.3
500	4.1	5.7	7.1
600	2.4	4.2	5.7

Table 6: The signal significance for different values of μ for three different integrated luminosities of 1, 2 and 3 ab^{-1} at the 14 TeV LHC.

cut-flow analysis for the signal and backgrounds, we estimate the significance of the signal, using Eq. 12, for various values of μ and for three different values of integrated luminosities 1, 2 and 3 ab^{-1} . The numbers for the significance have been presented in Table 6. For a light LSP of $M_{\tilde{\chi}_1^0} \sim 400$ GeV, it would be possible to discover them with more than 5σ significance at 1 ab^{-1} of integrated luminosity. On the other hand, for a heavy LSP $M_{\tilde{\chi}_1^0} \sim 600$ GeV, it will need around 3 ab^{-1} of data to have sufficient discovery prospects.

In Fig. 11 we show the statistical significance for the signal in the plane of $(M_2, \tan\beta)$ for two different values of $\mu = 300$ (left) and 500 GeV (right). As mentioned earlier, $\text{Br}(\tilde{\chi}_1^0 \rightarrow \nu h)$ also depends on parameters $\tan\beta$ and M_2 other than μ . The partial width in individual decay mode of the LSP depends on ratio of M_2/M_1 and $\tan\beta$ on such a way that the branching ratio to νh is minimum when $M_2/M_1 \approx 1$. Strictly speaking

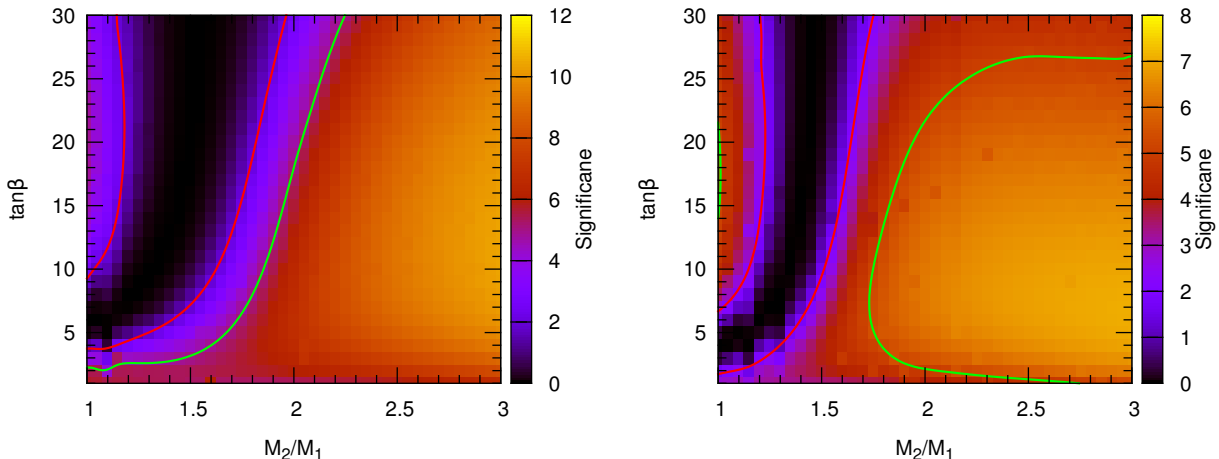


Figure 11: The signal significance in the $(M_2, \tan \beta)$ plane for two values of $\mu = 300$ GeV (left) and 500 GeV (right) at the 14 TeV LHC. For $\mu = 300$ GeV (500 GeV), integrated luminosities of 1 ab^{-1} (3 ab^{-1}) has been taken for the analysis. The region outside the red and green curves show the regions of the 2σ exclusion and the 5σ discovery, respectively.

this depends on $\tan \beta$ as well. This is also evident from Fig. 2. The dark regions in the figures denote the regions for low discovery prospects while the brighter region has better prospects to observe a Higgsino LSP in di-Higgs process. For $\mu = 300$ GeV, we find that it would be possible to discover the Higgsino-like LSP in di-Higgs production process at the LHC with only 300 fb^{-1} of integrated luminosity and a large portion of the parameter can be excluded at 2σ with 1 ab^{-1} . The region of exclusion has been shown by red curves in the figures. The 5σ discovery prospect has been denoted by green curves in both the plots. For $\mu = 500$ GeV, the 5σ discovery can only be obtained with full data set of the 14 TeV LHC *viz.* 3 ab^{-1} for large values of M_2 .

5 Summary and Conclusions

Motivated by the naturalness, we study a Bilinear RpV SUSY scenario where the LSP is Higgsino-like, and BRpV couplings determine the tree-level neutrino mass matrix. We investigate the parameter space of this scenario and study the decay patterns of the Higgsino LSP. We find that in a large part of the parameter space, the LSP decays to νh with branching fraction larger than 0.9. A large region of this yet unexplored parameter space can still be insensitive to the existing constraints coming from the LHC searches. We then study the pair production of the electroweakinos followed by the decays $\tilde{\chi}_1^\pm \rightarrow \tilde{\chi}_1^0 W^{\pm*}$ and $\tilde{\chi}_1^0 \rightarrow \nu h$. This leads to a very interesting signature of Higgs boson pair

production at the LHC accompanied with significant missing transverse energy. This di-Higgs production in BRpV model, occurring in association with a large missing transverse energy, is in distinct contrast to the Higgs boson pair production in the SM. This fact makes this signal quite feasible to search at the luminosity improved version of the 14 TeV LHC despite having a very small cross section.

Among the various decay channels for di-Higgs, we focus on the scenario where one of the Higgses decays to diphoton and the other decays to a bottom pair. This particular decay has the advantage of manageable SM backgrounds. Thus the signal which we are looking for includes 2 photons, 2 b jets and large missing transverse energy. We perform a realistic detector level simulation for the signal $\gamma\gamma b\bar{b} + \cancel{E}_T$ taking some benchmark points in the parameter space at the 14 TeV LHC. We also perform a full systematic study of all the background processes. It is found that the cuts on \cancel{E}_T and ΔR are instrumental in eliminating the QCD multijet backgrounds and suppressing the total background. We also notice that even though the cross sections for the signal decrease as the masses of the Higgsinos get heavy, the increased efficiency of the \cancel{E}_T and ΔR cuts helps to compensate the overall signal to background ratio. Finally we conclude that the LSP of mass 300-500 GeV would be amenable to discovery in the early LHC14 data in the di-Higgs channel. On the other hand for the heavy LSP ~ 600 GeV, it would require full data set (3 ab^{-1}) of 14 TeV run to have reasonable discovery prospects.

Acknowledgment: EJC is supported by the NRF grant funded by the Korea government (MSIP) (No. 2009-0083526) through KNRC at Seoul National University.

Appendix A: Effective R-parity violating vertices

Neutrino-neutralino diagonalization

Rotating away the neutrino-neutralino mixing mass terms (by θ^N) can be made by the following redefinition of neutrinos and neutralinos:

$$\begin{pmatrix} \nu_i \\ \chi_j^0 \end{pmatrix} \longrightarrow \begin{pmatrix} \nu_i - \theta_{ik}^N \chi_k^0 \\ \chi_j^0 + \theta_{ij}^N \nu_l \end{pmatrix} \quad (13)$$

where (ν_i) and (χ_j^0) represent three neutrinos (ν_e, ν_μ, ν_τ) and four neutralinos ($\tilde{B}, \tilde{W}_3, \tilde{H}_1^0, \tilde{H}_2^0$) in the flavor basis, respectively. The rotation elements θ_{ij}^N are given by

$$\begin{aligned} \theta_{ij}^N &= \xi_i c_j^N c_\beta - \epsilon_i \delta_{j3} \quad \text{and} \\ (c_j^N) &= \frac{M_Z}{F_N} \left(\frac{s_W M_2}{c_W^2 M_1 + s_W^2 M_2}, -\frac{c_W M_1}{c_W^2 M_1 + s_W^2 M_2}, -s_\beta \frac{M_Z}{\mu}, c_\beta \frac{M_Z}{\mu} \right) \end{aligned} \quad (14)$$

where $F_N = M_1 M_2 / (c_W^2 M_1 + s_W^2 M_2) + M_Z^2 s_{2\beta} / \mu$. Here $s_W = \sin \theta_W$ and $c_W = \cos \theta_W$ with the weak mixing angle θ_W .

Charged lepton/chargino diagonalization

Defining θ^L and θ^R as the two rotation matrices corresponding to the left-handed negatively and positively charged fermions, we have

$$\begin{pmatrix} e_i \\ \chi_j^- \end{pmatrix} \rightarrow \begin{pmatrix} e_i - \theta_{ik}^L \chi_k^- \\ \chi_j^- + \theta_{lj}^L e_l \end{pmatrix} \quad ; \quad \begin{pmatrix} e_i^c \\ \chi_j^+ \end{pmatrix} \rightarrow \begin{pmatrix} e_i^c - \theta_{ik}^R \chi_k^+ \\ \chi_j^+ + \theta_{lj}^R e_l^c \end{pmatrix} \quad (15)$$

where e_i and e_i^c denote the left-handed charged leptons and anti-leptons, $(\chi_j^-) = (\tilde{W}^-, \tilde{H}_1^-)$ and $(\chi_j^+) = (\tilde{W}^+, \tilde{H}_2^+)$. The rotation elements $\theta_{ij}^{L,R}$ are given by

$$\theta_{ij}^L = \xi_i c_j^L c_\beta - \epsilon_i \delta_{j2}, \quad \theta_{ij}^R = \frac{m_i^e}{F_C} \xi_i c_j^R c_\beta \quad \text{and} \quad (16)$$

$$(c_j^L) = -\frac{M_W}{F_C} (\sqrt{2}, 2s_\beta \frac{M_W}{\mu}),$$

$$(c_j^R) = -\frac{M_W}{F_C} (\sqrt{2}(1 - \frac{M_2}{\mu} t_\beta), \frac{M_2^2 c_\beta^{-1}}{\mu M_W} + 2 \frac{M_W}{\mu} c_\beta)$$

and $F_C = M_2 + M_W^2 s_{2\beta} / \mu$.

Sneutrino/neutral Higgs boson diagonalization

Denoting the rotation matrix by $\theta_i^S = a_i$, we get

$$\begin{pmatrix} \tilde{\nu}_i \\ H_1^0 \end{pmatrix} \rightarrow \begin{pmatrix} \tilde{\nu}_i + a_i H_1^0 \\ H_1^0 - a_i \tilde{\nu}_i \end{pmatrix} \quad (17)$$

With the expressions for the rotation matrices, we can obtain the effective R-parity violating vertices from the usual R-parity conserving interaction vertices, which are relevant to the LSP decays. We list them below by taking only the linear terms in θ 's which are enough for our purpose.

$\chi^0 - l - W$ vertices:

$$\mathcal{L}_{\chi^0 l W} = \overline{\chi_i^0} \gamma^\mu [P_L L_{ij}^{\chi^0 l W} + P_R R_{ij}^{\chi^0 l W}] e_j W_\mu^+ + h.c. \quad (18)$$

$$\text{with } L_{ij}^{\chi^0 l W} = \frac{g}{\sqrt{2}} [c_1^N, c_2^N - \sqrt{2}c_1^L, c_3^N - c_2^L, c_4^N] \xi_j c_\beta$$

$$R_{ij}^{\chi^0 l W} = \frac{g}{\sqrt{2}} [0, -\sqrt{2}c_1^R, 0, -c_2^R] \frac{m_j^e}{F_C} \xi_j c_\beta$$

$\chi^0 - \nu - Z$ vertices:

$$\mathcal{L}_{\chi^0 \nu Z} = \overline{\chi_i^0} \gamma^\mu P_L L_{ij}^{\chi^0 \nu Z} \nu_j Z_\mu^0 + h.c. \quad (19)$$

$$\text{with } L_{ij}^{\chi^0 \nu Z} = \frac{g}{2c_W} [c_1^N, c_2^N, 0, 2c_4^N] \xi_j c_\beta.$$

$\chi^0 - \nu - h$ vertices:

$$\begin{aligned}\mathcal{L}_{\chi^0\nu h} &= \overline{\chi_i^0} P_L L_{ij}^{\chi^0\nu h} \nu_j h + h.c. \\ \text{with } L_{ij}^{\chi^0\nu h} &= \frac{g}{2c_W} [s_W(1 - c_3^N c_\beta + c_4^N s_\beta), -c_W(1 - c_3^N c_\beta + c_4^N s_\beta), \\ &\quad (s_W c_1^N - c_W c_2^N) c_\beta, (s_W c_1^N - c_W c_2^N) s_\beta] \xi_j c_\beta\end{aligned}\quad (20)$$

$\chi^+ - \nu - W$ vertices:

$$\begin{aligned}\mathcal{L}_{\chi^+\nu W} &= \overline{\chi_i^+} \gamma^\mu [P_L L_{ij}^{\chi^+\nu W} + P_R R_{ij}^{\chi^+\nu W}] \nu_j W_\mu^- + h.c. \\ \text{with } L_{ij}^{\chi^+\nu W} &= \frac{g}{\sqrt{2}} [c_1^L - \sqrt{2} c_2^N, c_2^L - c_3^N] \xi_j c_\beta \\ R_{ij}^{\chi^+\nu W} &= \frac{g}{\sqrt{2}} [-\sqrt{2} c_2^N, c_4^N] \xi_j c_\beta\end{aligned}\quad (21)$$

$\chi^+ - l - Z$ vertices:

$$\begin{aligned}\mathcal{L}_{\chi^+ l Z} &= \overline{\chi_i^+} \gamma^\mu [P_L L_{ij}^{\chi^+ l Z} + P_R R_{ij}^{\chi^+ l Z}] e_j Z_\mu^0 + h.c. \\ \text{with } L_{ij}^{\chi^+ l Z} &= \frac{g}{2c_W} [c_1^L, 0] \xi_j c_\beta, \\ R_{ij}^{\chi^+ l Z} &= \frac{g}{2c_W} [2c_1^R, c_2^R] \frac{m_j^e}{F_C} \xi_j c_\beta,\end{aligned}\quad (22)$$

$\chi^+ - l - h$ vertices:

$$\begin{aligned}\mathcal{L}_{\chi^+ l h} &= \overline{\chi_i^+} [P_L L_{ij}^{\chi^+ l h} + P_R R_{ij}^{\chi^+ l h}] e_j h + h.c. \\ \text{with } L_{ij}^{\chi^+ l h} &= \sqrt{2} g [c_2^L c_\beta + 1, c_1^L s_\beta] \xi_j c_\beta \\ R_{ij}^{\chi^+ l h} &= [\sqrt{2} g c_2^R s_\beta - c_1^L c_\beta \frac{F_C}{v c_\beta}, \sqrt{2} g c_1^R c_\beta - (c_2^L c_\beta + 1) \frac{F_C}{v c_\beta}] \frac{m_j^e}{F_C} \xi_j c_\beta.\end{aligned}\quad (23)$$

Appendix B: Decay widths of neutralinos

For a generic decay process $\tilde{\chi}_i \rightarrow L_j V$ where L is either ν or ℓ^\pm and V is either Z or W^\pm , the decay width can be written as:

$$\Gamma(\tilde{\chi}_i \rightarrow L_j V) = \frac{G_F m_\chi^3}{4\sqrt{2}\pi} \left[|C_i^L|^2 + |C_i^R|^2 \right] |\xi_j|^2 c_\beta^2 I_2(r_V) \quad (24)$$

where C_i^L and C_i^R are the left- and right-handed couplings, r_V is (m_V^2/m_χ^2) and $I_2(r_V) = (1 - r_V)^2 \times (1 + 2 r_V)$.

1. For $\tilde{\chi}_i^0 \rightarrow \nu_j Z$

$$\begin{aligned}C_i^L &= \frac{1}{2} [N_{i1} c_1^N + N_{i2} c_2^N + N_{i4} 2c_4^N] \\ C_i^R &= 0\end{aligned}\quad (25)$$

2. For $\tilde{\chi}_i^0 \rightarrow \ell_j W$

$$\begin{aligned} C_i^L &= \frac{1}{\sqrt{2}} \left[N_{i1} c_1^N + N_{i2} (c_2^N - \sqrt{2} c_1^L) + N_{i3} (c_3^N - c_2^L) + N_{i4} c_4^N \right] \\ C_i^R &= \left[9N_{i2} c_1^R + \frac{N_{i4}}{2} c_2^R \right] \frac{m_j^e}{F_C} \end{aligned} \quad (26)$$

Similarly, for the decay $\tilde{\chi}_i^0 \rightarrow \nu_j h$, the decay width can be written as

$$\Gamma(\tilde{\chi}_i^0 \rightarrow \nu_j h) = \frac{G_F m_\chi m_W^2}{4\sqrt{2}\pi} \left[|C_i^L|^2 + |C_i^R|^2 \right] |\xi_j|^2 c_\beta^2 (1 - r_h)^2 \quad (27)$$

where r_h is m_h^2/m_χ^2 .

$$\begin{aligned} C_i^L &= N_{i1} t_W (1 - c_3^N c_\beta + c_4^N s_\beta) + N_{i2} (-1 + c_3^N c_\beta - c_4^N s_\beta) \\ &\quad + N_{i3} (t_W c_1^N - c_2^N) c_\beta + N_{i4} (t_W c_1^N - c_2^N) s_\beta \\ C_i^R &= 0 \end{aligned} \quad (28)$$

Here, N is the 4×4 matrix and diagonalize the neutralino mass matrices.

References

- [1] L. Hall and Suzuki, Nucl. Phys. **B231**, 419 (1984); I.-H. Lee, Phys. Lett. **138B**, 121 (1984).
- [2] A. S. Joshipura and M. Nowakowski, Phys. Rev. **D51**, 2421 (1995); M. Nowakowski and A. Pilaftsis, Nucl. Phys. **B461**, 19 (1996); F. M. Borzumati, Y. Grossman, E. Nardi and Y. Nir, Phys. Lett. **B384**, 123 (1996); B. de Carlos and P.L. White, Phys. Rev. **D54**, 3427 (1996); A. Yu. Smirnov and F. Vissani, Nucl. Phys. **B460**, 37 (1996); R. Hempfling, Nucl. Phys **B478**, 3 (1996); H.P. Nilles and N. Polonsky, Nucl. Phys. **B484**, 33 (1997); E. Nardi, Phys. Rev. **D55**, 5772(1997); M. Drees, *et al.*, Phys. Rev. **D57**, 5335 (1998); E.J. Chun, *et al.*, Nucl. Phys. **B544**, 89 (1999); A.S. Joshipura and S.K. Vempati, Phys. Rev. **D60**, 09509 (1999); Phys. Rev. **D60**, 111303 (1999); K. Choi, *et al.*, Phys. Rev. **D60**, 031301 (1999); O. Kong, Mod. Phys. Lett. **A14**, 903 (1999); S. Rakshit, *et al.*, Phys. Rev. **D59**, 091701 (1999); R. Adhikari, G. Omanovic, Phys. Rev. **D59**, 073003 (1999); Y. Grossman and H.E. Haber, Phys. Rev. **D59**, 093008 (1999); D.E. Kaplan and A. Nelson, JHEP 0001:033 (2000); J.L. Chkareuli, *et al.*, Phys. Rev. **D62**, 015014 (2000); O. Haug, *et al.*, Nucl. Phys. **B565**, 38 (2000); S. Davidson and M. Losada, JHEP 0005:021 (2000); F. Takayama and M. Yamaguchi, Phys. Lett. **B476**, 116 (2000); A. Abada, S. Davidson and M. Losada,

- Phys. Rev. **D65**, 075010 (2002); A.S. Joshipura, R.D. Vaidya and S.K. Vempati, hep-ph/0203182.
- [3] B. Mukhopadhyaya, S. Roy and F. Vissani, Phys. Lett. **B443**, 191 (1998); A. Datta, B. Mukhopadhyaya and F. Vissani, Phys. Lett. **B492**, 324 (2000).
- [4] E.J. Chun and J.S. Lee, Phys. Rev. **D60**, 075006 (1999); S.Y. Choi, E.J. Chun, S.K. Kang and J.S. Lee, Phys. Rev. **D60**, 075002 (1999); E.J. Chun and S.K. Kang, Phys. Rev. **D61**, 075012 (2000).
- [5] M. Hirsch, M.A. Diaz, W. Porod, J.C. Romao and J.W.F. Valle, Phys. Rev. **D62**, 113008 (2000); W. Porod, M. Hirsch J.C. Romao and J.W.F. Valle, Phys. Rev. **D63**, 115004 (2001).
- [6] E. J. Chun, D. W. Jung, S. K. Kang and J. D. Park, Phys. Rev. D **66**, 073003 (2002); D. W. Jung, S. K. Kang, J. D. Park and E. J. Chun, JHEP **0408**, 017 (2004).
- [7] R. Kitano and Y. Nomura, Phys. Rev. D **73**, 095004 (2006). [hep-ph/0602096]; C. Brust, A. Katz, S. Lawrence and R. Sundrum, JHEP **1203**, 103 (2012) [arXiv:1110.6670 [hep-ph]]; M. Papucci, J. T. Ruderman and A. Weiler, JHEP **1209**, 035 (2012) [arXiv:1110.6926 [hep-ph]]; H. Baer, V. Barger, P. Huang, A. Mustafayev and X. Tata, Phys. Rev. Lett. **109**, 161802 (2012) [arXiv:1207.3343 [hep-ph]].
- [8] S. Gori, S. Jung and L. T. Wang, JHEP **1310**, 191 (2013) [arXiv:1307.5952 [hep-ph]]; T. Han, S. Padhi and S. Su, Phys. Rev. D **88**, no. 11, 115010 (2013) [arXiv:1309.5966 [hep-ph]]; Z. Han, G. D. Kribs, A. Martin and A. Menon, Phys. Rev. D **89**, no. 7, 075007 (2014) [arXiv:1401.1235 [hep-ph]]; H. Baer, V. Barger, D. Mickelson, A. Mustafayev and X. Tata, JHEP **1406**, 172 (2014) [arXiv:1404.7510 [hep-ph]]; G. Barenboim, E. J. Chun, S. Jung and W. I. Park, Phys. Rev. D **90**, no. 3, 035020 (2014) [arXiv:1407.1218 [hep-ph]]; B. S. Acharya, K. Boek, C. Pongkitivanichkul and K. Sakurai, JHEP **1502**, 181 (2015) [arXiv:1410.1532 [hep-ph]]; S. Gori, S. Jung, L. T. Wang and J. D. Wells, JHEP **1412**, 108 (2014) [arXiv:1410.6287 [hep-ph]]; C. Han, D. Kim, S. Munir and M. Park, JHEP **1504**, 132 (2015) [arXiv:1502.03734 [hep-ph]].
- [9] E. W. N. Glover and J. J. van der Bij, Nucl. Phys. B **309**, 282 (1988); T. Plehn, M. Spira and P. M. Zerwas, Nucl. Phys. B **479**, 46 (1996) Erratum: [Nucl. Phys. B **531**, 655 (1998)] [hep-ph/9603205].
- [10] A. Djouadi, W. Kilian, M. Muhlleitner and P. M. Zerwas, Eur. Phys. J. C **10**, 45 (1999) [hep-ph/9904287].

- [11] M. J. Dolan, C. Englert and M. Spannowsky, JHEP **1210**, 112 (2012) [arXiv:1206.5001 [hep-ph]]; M. J. Dolan, C. Englert, N. Greiner, K. Nordstrom and M. Spannowsky, Eur. Phys. J. C **75**, no. 8, 387 (2015) [arXiv:1506.08008 [hep-ph]]; G. Aad *et al.* [ATLAS Collaboration], Phys. Rev. D **92**, 092004 (2015) [arXiv:1509.04670 [hep-ex]].
- [12] S. Dawson and I. M. Lewis, Phys. Rev. D **92**, no. 9, 094023 (2015) [arXiv:1508.05397 [hep-ph]].
- [13] B. Hespel, D. Lopez-Val and E. Vryonidou, JHEP **1409**, 124 (2014) [arXiv:1407.0281 [hep-ph]].
- [14] A. Azatov, R. Contino, G. Panico and M. Son, Phys. Rev. D **92**, no. 3, 035001 (2015) [arXiv:1502.00539 [hep-ph]].
- [15] J. Cao, Z. Heng, L. Shang, P. Wan and J. M. Yang, JHEP **1304**, 134 (2013) [arXiv:1301.6437 [hep-ph]].
- [16] M. van Beekveld, W. Beenakker, S. Caron, R. Castelijns, M. Lanfermann and A. Strubig, JHEP **1505**, 044 (2015) [arXiv:1501.02145 [hep-ph]].
- [17] L. Wu, J. M. Yang, C. P. Yuan and M. Zhang, Phys. Lett. B **747**, 378 (2015) [arXiv:1504.06932 [hep-ph]].
- [18] T. Binoth, S. Karg, N. Kauer and R. Ruckl, Phys. Rev. D **74**, 113008 (2006) [hep-ph/0608057]; A. Oliveira, arXiv:1404.0102 [hep-ph].
- [19] F. Gianotti *et al.*, Eur. Phys. J. C **39**, 293 (2005) [hep-ph/0204087].
- [20] K.A. Olive et al. (Particle Data Group), Chin. Phys. C **38**, 090001 (2014).
- [21] F. Staub, arXiv:0806.0538 [hep-ph].
- [22] W. Porod, Comput. Phys. Commun. **153**, 275 (2003) [hep-ph/0301101]; W. Porod and F. Staub, Comput. Phys. Commun. **183**, 2458 (2012) [arXiv:1104.1573 [hep-ph]].
- [23] T. Sjostrand, S. Mrenna and P. Z. Skands, JHEP **0605**, 026 (2006) [hep-ph/0603175].
- [24] G. Aad *et al.* [ATLAS Collaboration], Eur. Phys. J. C **73**, no. 3, 2306 (2013) [arXiv:1210.6210 [hep-ex]].
- [25] G. Aad *et al.* [ATLAS Collaboration], Eur. Phys. J. C **74**, no. 10, 3071 (2014) [arXiv:1407.5063 [hep-ex]].

- [26] ATLAS Collaboration, ATLAS NOTE, ATLAS-PHYS-PUB-2015-022.
- [27] G. L. Bayatian et al. (The CMS Collaboration), CMS Physics Technical Design Report, V.2: Physics Performance, CERN/LHCC 2006-02.